Performance Evaluation for Retrieving Aerosol Optical Depth from Directional Polarimetric Camera (DPC) based on GRASP Algorithm

Shikuan Jin [1], Yingying Ma [1, 2, *], Cheng Chen [4, 5], Oleg Dubovik [5], Jin Hong [6], Boming Liu [1], Wei Gong [2, 3]

[1] State Key Laboratory of Information Engineering in Surveying, Mapping and Remote Sensing, Wuhan University, China.
[2] Collaborative Innovation Center for Geospatial Technology, Wuhan 430079, China.
[3] School of Electronic Information, Wuhan University, China.
[4] GRASP-SAS, Remote Sensing Developments, Cite Scientifique, 59655 Villeneuve d'Ascq, France.
[5] Univ. Lille, CNRS, UMR 8518 - LOA - Laboratoire d'Optique Atmosphérique, Lille, France.
[6] Anhui Institute of Optics and Fine Mechanics, Chinese Academy of Sciences, Hefei 230031, China.

Corresponding Author: Yingying Ma (yym863@whu.edu.cn)

Abstract

Aerosol spatial distribution obtained from satellite sensors is critical for understanding regional aerosol environments, anthropogenic aerosol emissions, and global climate change. Directional Polarimetric Camera (DPC) is the first generation of multi-angle polarized sensor developed by China. It is onboard GaoFen-5 satellite, running in 705 km sun-synchronous orbit with a 13:30 pm ascending node. The sensor has three polarized channels at 490, 670, and 865 nm and ~9 viewing angles, mainly used for observing aerosols. The spatial resolution is ~ 3.3 km at nadir and global coverage is in ~2 days. In this study, the performance of aerosol optical depth (AOD) retrievals from the DPC/GaoFen-5 using the Generalized Retrieval of Atmosphere and Surface Properties (GRASP) algorithm were evaluated on a global basis for the first time. The results showed that the DPC GRASP/Models scheme, which used several aerosol-type mixings, achieved good performance. By comparing with AERONET observations, the correlation coefficient (R), root mean square error, and Expected Error (EE%, $\pm(0.05+0.15*AOD)$) were 0.9007, 0.0662, and 82.54%, respectively. The scattering angle, number of averaged pixels, length of timesteps, and radiative and polarized fitting residuals showed impacts on the results of AOD retrieval in the DPC GRASP/Models. From the most of AERONET sites, the R and EE% were larger than ~0.9 and ~80%. Compared with MODIS products, the spatial and temporal variations of aerosol could be caught by the DPC with the GRASP/Models, showing a good performance. However, values of AOD were also underestimated by DPC, probably due to overstrict cloud mask. The above findings validated the ability of DPC sensor to monitor aerosols. It should contribute to the development of aerosol parameter retrieval from multi-angular polarized sensors in the future.

Key Words: GRASP/Models, Aerosol Optical Depth, Directional Polarimetric Camera, GaoFen-5,

41   Aerosol Parameter Retrieval

1. Introduction

43   Aerosol is one of the most important components in the atmosphere. They influence the global
44   radiation budget balance and climate directly by scattering and absorbing incoming solar radiation
45   and indirectly by changing cloud microphysical properties (Albrecht 1989; Rosenfeld et al. 2008).
46   Due to the different emission sources and relatively transitory lifecycle in the atmosphere, aerosol
47   particles show large spatiotemporal variability, and are difficult to describe uniformly at a global
48   scale (Eck et al. 2010; Jin et al. 2019; Ma et al. 2021). This property can further affect atmospheric
49   motions, the hydrological cycle, and probably contribute to regional extreme weather events (Guo
50   et al. 2016; Li et al. 2016; Nakajima et al. 2007; Shi et al. 2021). Therefore, the development of
51   aerosol measurement technologies has received widespread attention in recent decades.

52   Satellite observation is the main approach to monitor and quantify aerosol distributions at a
53   global scale (Kaufman et al. 1997). Traditional satellite technology relies on prior assumptions about
54   the properties of the surface and atmosphere, because the prerequisite for successful retrieval of
55   aerosol is that the aerosol signal should be isolated from the remainder of the signal received by
56   satellite, which includes the combined effect from molecule, aerosol, cloud, and the underlying
57   surface (Lenoble et al. 2013). For instance, the appropriate spatial resolution helps to observe
58   aerosol through clear holes in otherwise cloudy skies (Jin et al. 2021). The choice of spectral channel
59   and bandwidth can avoid impact by gas absorption in narrow spectral bands known as atmosphere
60   window regions. More importantly, the spectral channel should be set in a carefully selected band
61   to avoid introducing uncertainty from underlying surface features, such as vegetation, bright desert,
62   and ocean color (Hsu et al. 2004; McCormick et al. 1979; Rao et al. 1989). Based on these principles,
63   a series of aerosol products from different sensors have been released, and they greatly promote the
64   developments of studies in aerosol-related fields, including aerosol climate effect, interaction of
65   aerosol and cloud, air quality and public health, and global climate modeling (Gao et al. 2017; Liu
66   et al. 2022; Sayer et al. 2013; Tegen and Lacis 1996; Zhang et al. 2021).

67   With the progress of satellite technology, sensors with broader spectral range, multiple angles,
68   and polarization observations have been applied to aerosol observations (Dubovik et al. 2019).
69   POLDER-3 is the third sensor in the POLarization and Directionality of the Earth's Reflectance
70   series, carried on the Polarization and Anisotropy of Reflectances for Atmospheric Science coupled
71   with Observations from a Lidar (PARASOL), which was launched on December 18, 2004, as part
72   of the A-Train (Tanre et al. 2011). This instrument views (±51° along track and ±43° across track)
73   Earth from ~14 different angles by using a set of wide-field telecentric optics and a rotating filter
74   wheel in nine spectral channels from 443 to 1020 nm (Deschamps et al. 1994). Among them, three
75   channels at 490, 670, and 865 nm have polarization observation capabilities. POLDER-3 provides
76   the longest multi-angle polarimetric observation record of the Earth-atmosphere system in space to
77   date and the PARASOL mission was terminated in December 2013 due to limited on-board fuel.
78   The Directional Polarimetric Camera (DPC) is the first Chinese multi-angle polarized Earth
79   observation satellite sensor, onboard the fifth satellite (GaoFen-5) of the Chinese High-resolution
80   Earth Observation Program (Li et al. 2018). It was launched successfully on May 9, 2018, with the
81   purposes of measuring aerosol parameters and providing information for the assessment of urban
82   air pollution. The design of DPC is similar to the POLDER-3. It is equipped with five non-polarized

bands at 443, 565, 763,765, and 910 nm and three polarized bands at 490, 670, and 865 nm, with relatively higher spatial resolution of 3.3 km, that can observe Earth from ~9 different angles. Therefore, the DPC occupies an important position in the development of polarization instruments in China, and is expected to provide beneficial information for atmospheric aerosol monitoring and satellite payload research.

The multi-angular polarized sensor can provide many more observations for the same pixel in an aerosol parameter retrieval . Compared to traditional spectral measurement, the multi-angle can help constrain bidirectional reflections function, reducing uncertainty from the surface (Diner et al. 1998), while the polarized signal is mainly from atmospheric aerosol and sensitive to particle microphysical properties (Mishchenko and Travis 1997). Generally, the polarized signal can be considered as an independent source of information. A well-known advantage is that the polarized light from the surface is accounts for a small part of the total polarized light compared with that from the particles and is mostly wavelength independent. In the algorithms for POLDER, the polarized signals at 670 and 865 nm are used for deriving the best aerosol model over the ocean and retrieving Aerosol Optical Depth (AOD) over land, due to the sensitivity to fine particles (Deuzé et al. 2001; Ge et al. 2020; Kacenelenbogen et al. 2006; Nadal and Bréon 1999). In addition, the existence of the cloudbow effect in the polarized signal can also be used to recognize cloud mask and detect cloud structure (Breon and Colzy 1999; Breon and Goloub 1998; Li et al. 2021).

However, the algorithms that retrieve aerosol parameters from only one or two polarized channels struggle to obtain complex aerosol optical and microphysical parameters, such as aerosol size distribution and absorbing and scattering properties. To solve this problem, the Generalized Retrieval of Atmosphere and Surface Properties (GRASP) algorithm was developed, which provides a statistical optimized strategy that allows all aerosol-related measurement data from multi-angular polarized sensors to participate in the retrieval (Dubovik et al. 2014). It points out that the measured redundancy provided by multi-angular polarized sensor is considered to be positive and useful, especially when the number of observations is larger than the unknowns (Dubovik et al. 2011). At present, the GRASP algorithm has been successfully applied to a variety of sensors, including POLDER, lidar, and sun photometer, to retrieve complex aerosol parameters (Chen et al. 2020; Li et al. 2019; Lopatin et al. 2021). In this study, we retrieved AOD from DPC observations by using GRASP algorithm and evaluated possible error influencing factors. At the same time, by comparing MODIS and AERONET observations, the aerosol monitoring performance of DPC were verified in different space and time scales. This will partially lay the foundation for the retrieval of aerosol parameters from multi-angular polarized sensors in the future of China.

2. Satellite and Ground-based Data

2.1 DPC Data

The DPC is a multi-angular polarized sensor carried on the GF-5 satellite, which was launched in May 9, 2018. This sensor completes a scan of entire Earth's surface about every two days from a sun-synchronous orbit and provides a swath of 1850 km with a spatial resolution of 3.3 km (Li et al. 2018). The DPC contains eight bands from 443 to 910 nm with a bandwidth of 10-40 nm that can observe earth from ~9 different angles in a local time of ~13:30 PM. Along with channels for water vapor (910 nm) and pressure (Oxygen A band: 763 and 765 nm), five bands (443, 490, 565,

670, and 865 nm) are designed to measure aerosols (Li et al. 2018). The polarimetric capability at 490, 670, and 865 nm is realized by a polarized filter wheel (0°, 60°, and 120°) and a step motor (Hagolle et al. 1999). The laboratory calibration uncertainties are 5% for normalized radiation and 0.02 for Degree Of Linear Polarization (DOLP) (Li et al. 2021). An in-flight calibration study showed that the radiometric calibration error increased to ~9% at 865 nm and the polarimetric calibration error increases to ~0.04 at 490 and 670 nm after launch, by respectively applying Rayleigh and glint scenes over ocean (Qie et al. 2021). Degradation of instrument performance over time may result in higher negative radiometric shift (Zhu et al. 2022). Thus, additional correction coefficients were also applied in this study to correct the image of the DPC observations from March to April, 2020. The processing of DPC data is described in Section 3.2 in detail.

2.2 MODIS aerosol products

The Moderate-resolution Imaging Spectroradiometer (MODIS) has been in service for over two decades, providing valuable Earth's observations. The MODIS Level 2 C6.1 aerosol product (MxD04) is generated by using Dark Target (DT) algorithm and Deep Blue (DB) algorithm (Hsu et al. 2013; Levy et al. 2013). It provides multi-wavelength AOD data from each individual image with spatial resolutions of 3 km and 10 km. The MODIS Level 2 C6 aerosol product (MCD19A2) calculates aerosol parameters by using the Multi-Angle Implementation of Atmospheric Correction (MAIAC) algorithm from the continuous scenes of two satellites (Terra and Aqua) and considers temporal and spatial correlation of aerosols, with spatial resolution of 1 km (Lyapustin et al. 2018). DT algorithm provides retrievals over ocean and land except for bright surfaces (such as desert dust), while the DB algorithm is only applied over land, and the MAIAC algorithm is used over land and part of the surrounding ocean. These MODIS aerosol products have been rigorously tested and verified, and are widely used in aerosol-related studies (Che et al. 2019; Sayer et al. 2014; Zhdanova et al. 2020). In this study, the corrected AOD (quality flag = 3) on land and average AOD (quality flag = 1,2,3) on the ocean are selected from the DT products. The best estimated AOD (quality flag = 2,3) is selected in the DB products. The best quality AOD (QA AOD = 0000) is selected in the MAIAC products.

2.3 AERONET observations

The AErosol RObotic NETwork (AERONET) is a federation of ground-based remote sensing aerosol networks, established and expanded by various institutions from different countries (Holben et al. 1998). It has contributed continuous and long-term aerosol optical, microphysical, and radiative properties for more than 25 years in major ecosystems and human activity areas around the world. The AOD data used for validation were acquired from 178 AERONET sites with Level 2.0 AOD products, which have been cloud-screened and quality controlled. The uncertainties of AOD are less than 0.02 (Eck et al. 1999). In order to match the AERONET data to the satellite observations, a common approach is followed to averages satellite data within ±30 min and a circle of 0.25° (~25 km) radius centered at the selected site (Sayer et al. 2013). The relationship between multi-wavelength AOD proposed by Ångstrom (1964) was applied to calculate the AOD at corresponding wavelength of satellite bands from AERONET data.

3. Methods

3.1 Introduction of GRASP algorithm

GRASP is an open-source software package (https://www.grasp-open.com/) for calculating and retrieving various optical and microphysical properties of aerosol and surface from observations of different remote sensing instruments, such as satellite, lidar, radiometer, and radiosonde (Dubovik et al. 2021). It was originally designed to solve the problem of aerosol retrieval from the PARASOL observations (Dubovik et al. 2014), while now has become a scientifically rigorous and versatile algorithm based on generalization principles that works with diverse remote sensing applications in the community after continuous development (Dubovik et al. 2021). The GRASP algorithm contains two pivotal and independent modules. One is used to calculate the scattering, absorption, and extinction of light between different media from the physical level, simulating theoretical observational radiation signal, called "Forward Model". It allows definition of various complex aerosol (size distribution, refractive index, and sphere fraction, etc.) and surface properties (Bidirectional Reflectance/ Polarization Distribution Function, BR/PDF, etc.) in the construction of model. Therefore, it is possible to transform from optical observations to aerosol microphysical properties and estimate the surface parameters (Dubovik et al. 2011). The other module can be thought of as general mathematical operations without any particularly physical nature, called "Numerical Inversion". It follows the statistically optimized strategy to fit observations under the fundamental frameworks of the Maximum Likelihood Method and multi-term Least Square Method (Dubovik and King 2000). GRASP also realizes multiple-pixel retrieval, which constrains the variability of aerosol and surface optical properties in fitting process by an extra prior knowledge. Due to the consideration of the surrounding pixel information, the multi-pixel retrieval is more stable, and more importantly, it can make up for the lack of aerosol reflection information in some cases, such as conditions that the signal from aerosol is much less than that from the surface (Dubovik et al. 2011). Based on the above advantages, the GRASP supports input measurements/parameters from different sources and levels, such as normalized and polarized radiance, vertical extinction and backscatter profile, and optical depth. This avoids that the most popular look-up table-based methods are difficult to apply to each other, due to the limitations of different sensor channel and characteristic.

3.2 Pre-processing of DPC Data

In order to partially offset the signal attenuation due to instrument aging, before the pre-processing and retrieval, the radiance signals from the DPC were transferred and corrected to normalized radiative and polarized reflectance at top of the atmosphere, as equation 1.

$$[I_N, Q_N, U_N]^T = \pi \cdot [I, Q, U]^T / [E_0 \cdot A'_k(\theta_0) \cdot P'_k(\theta)] \qquad (1)$$

where, the $[I, Q, U]^T$ are represent the radiative and polarized radiances, received by the DPC, in the form of the first three parts of the Stokes vector. The $A'_k(\theta_0)$ and $P'_k(\theta)$ are the two additional correction coefficients. For I, they are applied following the results of Zhu et al. (2022), which depends on the view zenith angle (θ) and calculated based on Rayleigh scenes over sea surface. For polarimetric signals, the additional correction coefficients can be referred to Qie et al. (2021). The E_0 is the standard solar radiation flux and the $[I_N, Q_N, U_N]^T$ are the corrected normalized signals at top of the atmosphere of DPC.

In successful AOD retrieval, one of the key processes is to screen appropriate pixels. Cloud pixel is the main factor impacting aerosol retrieval, because they will block the signal from aerosol due to high reflectance, large coverage, and relatively high vertical position. Even very thin cirrus clouds and missed cloud edges can cause an positive error of ~13% in visible channel (Koren et al. 2007). To remove cloud pixels in DPC images, we used several universal methods by considering cloud-sensitive characteristics in radiative and polarized bands:

1) The first step is to filter the image with a 3×3 sliding window at the blue (490 nm) and red (670 nm) bands for land and sea surfaces, respectively (Remer et al. 2012). If the standard deviation of a window is greater than 0.0025, then the center pixel will be marked as a cloud pixel and removed (Martins et al. 2002). This method was initially applied to the MODIS image by considering the spatial variability of aerosol and cloud pixels. In addition, a threshold of > 0.4 in the green (565 nm) band is also used to detect cloud pixels after the filter process, in accordance with the DT algorithm. This threshold is to exclude very uniformly distributed cloud pixels in the central area of thick clouds, and some snow pixels and glint area will also be excluded at the same time.

2) In second step, a whiteness test was applied by using reflectance in visible bands. It uses the characteristic that clouds are white in the visible band, considering that pixel with the absolute value of relative deviations greater than 0.7 is cloud, as equation 2-3.

$$MeanVis = (Band_1 + Band_2 + Band_3)/3 \qquad (2)$$

$$Whiteness\ Test = \sum_{i=1}^{3} |(Band_1 - MeanVis)/MeanVis| > 0.7 \qquad (3)$$

Where, $Band_1$, $Band_2$, and $Band_3$ are reflectance in red, green, and blue bands received by satellite at top of the atmosphere, respectively. Corresponding to the DPC, they are 490, 565, and 670 nm, respectively. In the absence of infrared and thermal infrared information, it can supplementally remove any pixels that have flat reflectance, similar to some operators using reflectance ratio to detect clouds. This method was proposed by Gomez-Chova et al. (2007) for Medium Resolution Imaging Spectrometer (MERIS) multispectral image, and it has also been considered in the well-known Fmask algorithm (Zhu and Woodcock 2012).

3) The third step used polarized bands to remove cloud pixels, following a fact that cloud drops can show a relatively strong polarized reflectance by multiple scattering (cloudbow effect) under a specify observation geometry. This feature has been used to generate cloud mask product for both POLDER and DPC sensors (Breon and Colzy 1999; Li et al. 2021). When the scattering angle (SCA) is between 127° and 157°, pixels with corrected polarized radiation at 865 nm larger than 0.03 and 0.05 for ocean and surface, respectively, are defined as cloud (Li et al. 2021). The relatively large SCA range is for a strict screening, given that the main peak of the polarized reflectance by cloud water droplets is ~142° (Goloub and Deuze 1994). In addition, any obvious noise is also removed in this step, such as the case of DOLP > 1.

3.3 Construction of Multi-pixel Retrieval Unit

Next, we will explain the necessary operations and settings of parameters to apply the GRASP algorithm to DPC data in detail. The GRASP algorithm can use the temporal and spatial continuity of pixels, and allow a group of pixels to be inverted at the same time. The multi-pixel retrieval unit for DPC in the study is shown as **Figure 1**. Each small cube represents a pixel in geographic grids with a spatial resolution of 0.1°×0.1° (3×3 DPC pixel averaged). This is in accordance with the MODIS 04_L2 product (~10 km). The projection is determined by the DPC data. Each pixel is guaranteed to have at least 3 different observation angles. Size of the retrieval unit can be arbitrarily

247 selected, but is limited by the hardware memory. Different colors show the percentage of land or
248 sea, and usually do not change with time. They need to be clearly defined in GRASP to select
249 different surface reflectance models. Cloud and no-data pixels need to be removed before the
250 retrieval, because the cloud flag setting has not been implemented in the current version of code.
251 Finally, this retrieval unit was processed using the GRASP algorithm to derive the AOD
252 distributions.

253   3.4 Settings of Retrieval Parameters

254   The settings of initial value and spatial-temporal constraint can significantly impact results of
255 the statistically optimized strategy in the GRASP algorithm (Dubovik et al. 2011). The GRASP
256 allows several strategies to fit observations. For instances, the GRASP software gives two retrieval
257 schemes for POLDER observations. The configurations of the two schemes are different only by
258 settings of aerosol size distribution in the forward model. One fits the aerosol size distribution with
259 16 triangle bins from the range of 0.05 to 15.0 μm, while the other uses 5 lognormal bins at 0.1,
260 0.1732, 0.3, 1.0, and 2.9 μm, based on pre-calculated optimized kernels of the POLDER-3. The 5
261 lognormal bins scheme increases speed by ~9 times (2.5GHz CPU) without any
262 graphical acceleration compared to the 16 triangle bins scheme, and it has been used to generate the
263 operational PARASOL/GRASP aerosol products (Chen et al. 2020). In addition, there is a scheme
264 that is being tested called "GRASP/Models". GRASP/Models approach assumes by externally
265 mixing several aerosol types with fixed optical parameters, which is fast and more stable AOD
266 retrieval especially when aerosol loading is low (Chen et al., 2020).

267   A tolerable absolute error in radiative transfer calculations is set to 0.0005 and the multiple
268 scattering effects have been considered. The number of atmospheric layers is set to 10 with an
269 exponential distribution. The input data of the GRASP algorithm was both normalized radiative
270 measurements at 443, 490, 565, and 670 nm and DOLP of 490 and 670 nm. The initial guess of
271 aerosol and surface properties are default in the GRASP software. They are applied to calculate
272 AOD at a global scale. The Ross-Li's model (Li and Strahler 1992) and the Cox-Munk model (Cox
273 and Munk 1954) were used for modeling radiative (non-polarized) reflectance over land and ocean,
274 respectively, while, the surface polarized reflectance followed the method of Nadal and Bréon
275 (1999). More details are documented in Dubovik et al. (2011). Among them, the complex refractive
276 index and surface properties are generally allowed to be fit as wavelength-dependent parameters in
277 iterations. All constraints on values are given a default sizeable range, such as the first parameter in
278 the Ross-Li's model allowed to vary from 0.001 to 1.100. By light scattering calculations (Dubovik
279 et al. 2006), all aerosol microphysical parameters are converted into optical parameters to participate
280 in radiative simulation. Spatial and temporal constraints of variabilities of aerosol and surface
281 properties are realized by using Lagrange multiplier method. More details can be referred to
282 Dubovik et al. (2021). In this study, the GRASP/Models scheme was used to retrieve AOD from
283 DPC. All calculations of the GRASP relied on the supercomputing system in the Supercomputing
284 Center of Wuhan University.

285 **4. Results and Discussions**

286   4.1 Validation of DPC/GRASP with AERONET

As shown in **Figure 2**, the AERONET observations were used as the references to estimate the performance of AOD retrieval from DPC images based on the GRASP algorithm. Linear regression, correlation coefficient (R), Root Mean Square Error (RMSE), Mean Bias (MB), percentage falling into Expected Error (EE%, ±(0.05+0.15*AOD)), and matching Number (N) were also calculated. Among them, the EE% is selected in accordance with the MODIS error envelop and the ideal EE% is ~68% under assumption of normal distribution within one sigma confidence interval. Overall, the DPC GRASP/Models AOD matches the AERONET observations with an R of 0.8511, a MB of 0.0256, and a RMSE of 0.0842, showing good performance without any quality control. Nearly 80% of the GRASP/Models AOD retrievals fall within the EE% bounds, revealing that the error envelop of DPC is probably narrower than that of MODIS. While, the slope of linear regression was 0.8686, less than 1. This means that under heavy aerosol loading, the DPC/GRASP probably underestimate the AOD. More details are presented in **Figure 2c**. It is found the lower slope of linear regression is mainly controlled by several points which have larger AOD (> 0.8). By contrast, when AOD is less than 0.8, the retrieval is stable.

In order to further study the retrieval performance of GRASP/Models and control the quality of the retrieval result from DPC data, we calculated the dependences of absolute MB with retrieval residuals, timesteps (serial length) and average pixel (involved in retrieval) number in retrieval units, and observation geometry, as shown in **Figure 3**. The retrieval absolute MB showed an obvious increase when the SCA is larger than 150°. Critical observation conditions, such as pixels at the edge of the image, will probably result to a larger error in both satellite sensor and forward model. By contrast, different viewing angle number (3-11) have relatively little impact on the retrieval results, with the absolute MB per bin ranging between 0.0296 and 0.0595. With increase in timesteps, the absolute MB showed a slightly decreasing trend, from 0.0543 to 0.0561. The same phenomenon was also found in the **Figure 3d**. The absolute MB decreased from 0.0691 to 0.0435 with the number of averaged pixels increasing. This indicated that the fitting scheme for using the external mixing of different aerosol types in this scheme of the GRASP/Models showed positive dependence of the length of timesteps and number of pixels. In addition, the spatial-temporal constraints in the retrieval are also affected by Lagrange multipliers, which can be customized in the configuration file.

Fitting residual is an important factor to estimate the quality of retrieval in GRASP. It was found that the absolute MB showed a slight increase (from 0.0397 to 0.0596) when the radiative fitting residuals were larger than 8%. While, the absolute MB had a trend to decrease first and then increase, with increase in the polarized fitting residuals. Given that the DPC designed uncertainty is about 5% for radiometric measurements and 0.02 for DOLP, the relatively large absolute MB (0.069) at 0.01 of the polarized fitting residuals is probably caused by the noise. To summarize, the SCA, number of averaged pixels, and fitting residuals showed the impacts on DPC GRASP/Models AOD retrieval in this test. Retrieval is considered low quality if any of the following conditions are met: 1) Pixels with SCA > 150; 2) number of averaged pixels < 4; 3) length of timesteps < 5; 4) non-polarized fitting residual > 8%; 5) polarized fitting residual > 0.06.

Figure 4a-b shows the scatterplots and density distributions of DPC/GRASP AOD versus the AERONET observations after quality control. About 20% of the points were removed. It was found that the performance of AOD retrieval from DPC images showed an enhancement. For DPC GRASP/Models, the R increased from 0.8511 to 0.9001, the EE% increased from 79.30% to 82.54%, the RMSE decreased from 0.0842 to 0.0662, and the MB decreased from 0.0256 to 0.0234. **Figure 4c** displayed the change of differences between DPC and AEROENT AOD. The underestimations

when AOD > 0.8 were not found to be restrained by the quality control. A possible reason is that an overly restrictive cloud mask can remove aerosol pixels during heavy pollution. In addition, the negative drift after the launch of the DPC may also be the reason, if it is not fully corrected.

4.2 Evaluation of DPC AOD Performance at a Spatial Scale

The DPC AOD retrieved by the GRASP/Models were compared with AERONET observations at each individual site to show a world-wide retrieval result as **Figure 5**. The R, RMSE, MB, and EE% were calculated and displayed for sites where the matching number of pixels was larger than 5. In addition to the observation performance of the DPC itself, spatial variations in performances of AOD retrieval greatly depend on settings of initial parameter and constraint in the GRASP, whether they are in line with the local aerosol and surface environments. Results showed that the GRASP/Models achieved a great performance in different regions. The high values of R (> 0.8) were found in most regions, while the several lower values (~0.6) were mainly observed in North America. The values of RMSE at most sites were less than 0.08. These suggest that most values of AOD retrieval matched the AERONET AOD very well. At several sites, such as Asia and Africa, the RMSE were larger than 0.2, revealing that the AOD has a relatively larger deviation calculated from DPC images based on current parameter setting with the GRASP algorithm in the regions. From the MB of **Figure 5c**, the values of AOD were overestimated (~0.04) in the most areas. By contrast, the underestimations were found in high aerosol loading regions, such as South Asia and North Africa, that MB values were between -0.02 and -0.10, in accordance with the large underestimation when AOD > 0.8 mentioned above. The EE% showed that over 80% of AOD retrieved in sites can fall within the expected error range. It is worth noting that the parameterization in the GRASP/Models scheme is a globally consistent configuration in this study and does not consider the characteristics between different regions. This means that it is possible to achieve better results in local regions by adjusting different parameterizations.

To further estimate the performance of DPC/GRASP AOD, two regions were selected as cases as shown in **Figure 6**. The MODIS MAIAC, DT, and DB aerosol products were used as comparisons. It was noted that the DB algorithm was only executed over land in the C6.1 MODIS DB aerosol products. It was found that the spatial coverage of GRASP/Models AOD from DPC over land was slightly lower than the MAIAC MODIS aerosol products. In addition to the narrower field of view and longer re-visit cycle on DPC (MODIS operated in two satellite: Terra and Aqua), the cloud mask method probably also mis-classified the cloud-free pixels in heavy aerosol loading conditions. This also partially resulted the underestimation of DPC AOD because the heavy aerosol loading pixels are removed. Nevertheless, DPC still properly captures the spatial distribution of AOD. The highest AOD values (> 1.0) in the southern part of China (mainly Guangdong and Guangxi) were caught by the current retrieval strategy. This is in accordance with the three MODIS products. By contrast, the AOD found in North China Plain and Centre China by the DPC GRASP/Models (~0.5) were a little bit lower than MAIAC and DT products (~0.6). However, the DT aerosol products showed higher AOD in this region, closed to ~1.0. This phenomenon owes to unsuitable aerosol models, which further results a persistent overestimation in DT algorithm (Che et al. 2019). By the additional radiometric and polarimetric correction, the DPC GRASP/Models showed good performance over both Land and Ocean. The high values of AOD in the South China Sea and the estuary of the Yangtze River can be clearly captured. To summarized, the DPC showed spatial ability of AOD retrieval based on GRASP algorithm in China region and the similar results have also been reported recently

374   by using the GRASP/component module (Li et al. 2022).

375   Another case was selected in Western Europe where the air is clean and aerosol loading is low
376   (< 0.2) in the most of time around year. As shown in **Figure 6b**, different satellites and aerosol
377   retrieval methods showed slightly different distributions of AOD. In addition to the different transit
378   times between DPC and MODIS, this phenomenon is also probably because the aerosol signal is
379   difficult to separate from the remainder of signal under low aerosol loading conditions and thus
380   result in relative larger uncertainties of retrieval. From the AOD maps of DPC GRASP/Models, the
381   relatively high values of AOD (~0.25) were found in Central France, Southern Spain, and Southern
382   England. While, the MODIS MAIAC showed lower AOD (~0.1) over the mainland and two points
383   of high AOD (~0.5) were found in Northern coastal areas of Spain and Algeria. By contrast, the
384   distributions of AOD calculated by DT and DB algorithm were also different from that calculated
385   by DPC GRASP/Models and MAIAC. The high AOD (~0.4) region appeared in Northern France,
386   Italy, and Southern England. Compared with single pixel-based retrieval algorithm (such as DT and
387   DB), the GRASP and MAIAC considered more temporal and spatial information of aerosol and
388   surface parameters. And benefit from the consistency of all assumptions (regarding aerosol and a
389   priori constrains), the DPC GRASP exhibits minimal land-sea contrast. All of them have been
390   proven to have good performance of AOD retrieval (Chen et al. 2020; Lyapustin et al. 2018; Ou et
391   al. 2021; Sayer et al. 2014).

392   **Figure 7** showed density distributions of difference between DPC and MODIS products in
393   ranges of AOD $\leq$ 0.2, 0.2 < AOD $\leq$ 0.7, and AOD > 0.7. Corresponding to the **Figure 6,** this is
394   used to complement quantitative evaluations for the two regions. It can be found a common pattern
395   showed in all sub-plots, namely that the differences were nearly normally distributed centered on
396   the 0 under low aerosol loading conditions (AOD $\leq$ 0.2). With increasing AOD (AOD > 0.7), the
397   differences showed an increasing negative bias, with the peak value varying from -0.5 to -1.0. The
398   DPC GRASP/Models underestimated AOD under heavy aerosol loading conditions, similar to the
399   comparisons with AERONET. In follow-up studies, a more detailed investigation of this problem is
400   required.

401   4.3 Comparison of DPC AOD with MODIS Products at a Temporal Scale

402   In this section, time-series of AOD were evaluated against MODIS aerosol products based on
403   the observations of AERONET site. The time-series of daily RMSE is calculated for the global
404   AERONET data set, as shown in **Figure 8**. Lower value of RMSE means the smaller actual errors,
405   indicating a good match with the AERONET. The AERONET stations had relatively continuous
406   observations during the study period to avoid that global validation statistics shift in local emphasis
407   and introduce temporal variation in the global results (Gupta et al. 2018). From the **Figure 8**, it was
408   found that the time series of AOD from DPC GRASP/Models had a good matching with the
409   AERONET AOD. The values of RMSE were ~0.06 and stable before 87th day. While the reason of
410   relatively large RMSE (~0.12) around 90th day is presumed to be heavy aerosol loading conditions,
411   as the DPC GRASP/Models would underestimate AOD under this situation. The similar temporary
412   rapid increases in RMSE were also found in MODIS products, such as the 80th day of the DT, the
413   85th day of the DB, and 98th day of the MAIAC. This reflects the time instability of algorithms. In
414   addition, the lowest daily averaged RMSE was found in DPC GRASP/Models with value of 0.0663,
415   and then MODIS DT (0.0863) and MODIS DB (0.0913). The low RMSE of DPC may be due to it
416   ignoring some high value AODs. It is worth noting that the same parameter scheme (including start

points and constraints) was applied globally in the GRASP/Models. Therefore, the difference in aerosol optical properties and spatial-temporal heterogeneity in different regions may be not considered appropriately. The optimization of the region is expected to improve the retrieval effect and further evaluation also requires the use of longer sequences of DPC data in the future.

Figure 9 showed three cases at different underlying surface to display the time series of AOD retrieved from DPC GRASP/Models on the basis of AERONET observations. The DT AOD was also compared as a reference, due to its stable performance. It was found that the behavior of AOD from DPC/GRASP and MODIS DT was generally consistent with AERONET at the three sites. From the scatterplots, the values of R were 0.947 and 0.949, 0.943 and 0.959, and 0.967 and 0.859 for MODIS DT and DPC GRASP/Models AOD at Raciborz, Magurele_Inoe, and FZJ-JOYCE, respectively. The GRASP/Models AOD retrieved from DPC were slightly higher than the AERONET in the FZJ-JOYCE site and thus it resulted a relatively lower R. Nevertheless, in general, DPC/GRASP has a good ability to capture the temporal variation of aerosols.

Conclusion and Summary

The DPC/GaoFen-5 is the first multi-angular polarized sensor launched by China and thus it has occupied an important position in the development of satellite sensors. In this study, AOD was retrieved from the DPC images by using the GRASP algorithm and compared with AERONET and MODIS observations. The main purpose is to evaluate the performance of the DPC to monitor global aerosols.

On a global basis, a uniform parameterization scheme, which defined the variation ranges and start values of the optical and microphysical properties (realized by aerosol type) of the aerosol, was applied in the "Model" module of GRASP. Validations against AERONET showed that the R and EE% of DPC GRASP/Models were 0.8511 and 79.30%, respectively, in the first attempt. The SCA, number of averaged pixels in retrieval units, and fitting residual showed an impact on the results of AOD. A larger number of pixels in retrieval units and a smaller fitting residual can help improve the quality of retrieval. By quality control (removing pixels: SCA > 150; number of averaged pixels < 4; length of timesteps < 5; non-polarized fitting residual > 8%; polarized fitting residual > 0.06), the R and EE% of DPC GRASP/Models AOD improve to 0.9007 and 82.54%, respectively. The corresponding MB and RMSE decreased from 0.0256 and 0.0842 to 0.0234 and 0.0662, respectively. This indicated that DPC has a good ability to detect aerosols under this scheme.

In the perspective of spatial scale, the R and EE% of GRASP/Models were larger than 0.9 and 80% respectively at the most AERONET sites. Large RMSE and Low EE% were found in heavy aerosol loading conditions such as Asia and Africa. When the actual AOD is large, the retrieval bias of AOD from satellite observations will be amplified as reflected in RMSE and EE% to some extent. By compared with MODIS aerosol products, the AOD from DPC GRASP/Models showed good consistency in China, with all heavy aerosol loading regions were detected. However, the values of AOD are underestimated by DPC, probably due to overstrict cloud mask. Evaluation of the time-serial AOD showed the performance of DPC GRASP/Models is similar to the MODIS DT and better than MODIS DB and MAIAC products. Therefore, to summarize, the DPC can capture spatial and temporal variations in aerosols. The study improves to our understanding of DPC and find a solution for retrieving AOD based on GRASP algorithm. The continuous development of multi-angle sensors polarized plays an important role in aerosol monitoring in the future.

Acknowledgement

This study was funded by the National Key R&D Program of China (Grant No. 2018YFB0504500), National Natural Science Foundation of China (Grant No. 41875038, No. 42071348, and No. 42001291), the Key R&D projects in Hubei Province (Grant No. 2021BCA220) and supported by the LIESMARS Special Research Funding. We are grateful to the Moderate Resolution Imaging Spectroradiometer (MODIS) Team, the Aerosol Robotic Network (AERONET) Organization and the GaoFen-5 Directional Polarimetric Camera (DPC) Developed Team for freely distributing their aerosol products and measurements. The numerical calculations in this paper have been done on the supercomputing system in the Supercomputing Center of Wuhan University. Finally, we would also like to thank all reviewers for their constructive and valuable comments.

References

Albrecht, B.A. (1989). AEROSOLS, CLOUD MICROPHYSICS, AND FRACTIONAL CLOUDINESS. *Science, 245*, 1227-1230, doi:10.1126/science.245.4923.1227

Ångstrom, A. (1964). The Parameter of Atmospheric Turbidity. *Tellus, 16*, 64-75, doi:10.3402/tellusa.v16i1.8885

Breon, F.M., & Colzy, S. (1999). Cloud detection from the spaceborne POLDER instrument and validation against surface synoptic observations. *Journal of Applied Meteorology, 38*, 777-785, doi:10.1175/1520-0450(1999)038<0777:cdftsp>2.0.co;2

Breon, F.M., & Goloub, P. (1998). Cloud droplet effective radius from spaceborne polarization measurements. *Geophysical Research Letters, 25*, 1879-1882, doi:10.1029/98gl01221

Che, H., Yang, L., Liu, C., Xia, X., Wang, Y., Wang, H., Wang, H., Lu, X., & Zhang, X. (2019). Long-term validation of MODIS C6 and C6.1 Dark Target aerosol products over China using CARSNET and AERONET. *Chemosphere, 236*, 124268, doi:10.1016/j.chemosphere.2019.06.238

Chen, C., Dubovik, O., Fuertes, D., Litvinov, P., Lapyonok, T., Lopatin, A., Ducos, F., Derimian, Y., Herman, M., Tanré, D., Remer, L.A., Lyapustin, A., Sayer, A.M., Levy, R.C., Hsu, N.C., Descloitres, J., Li, L., Torres, B., Karol, Y., Herrera, M., Herreras, M., Aspetsberger, M., Wanzenboeck, M., Bindreiter, L., Marth, D., Hangler, A., & Federspiel, C. (2020). Validation of GRASP algorithm product from POLDER/PARASOL data and assessment of multi-angular polarimetry potential for aerosol monitoring. *Earth System Science Data, 12*, 3573-3620, doi:10.5194/essd-12-3573-2020

Cox, C., & Munk, W. (1954). Measurement Of The Roughness Of The Sea Surface From Photographs Of The Suns Glitter. *Journal Of The Optical Society Of America, 44*, 838-850, doi:10.1364/JOSA.44.000838

Deschamps, P., Breon, F., Leroy, M., Podaire, A., Bricaud, A., Buriez, J., & Seze, G. (1994). The POLDER mission: instrument characteristics and scientific objectives. *Ieee Transactions on Geoscience and Remote Sensing, 32*, 598-615, doi:10.1109/36.297978

Deuzé, J.L., Bréon, F.M., Devaux, C., Goloub, P., Herman, M., Lafrance, B., Maignan, F., Marchand, A., Nadal, F., Perry, G., & Tanré, D. (2001). Remote sensing of aerosols over land surfaces from POLDER-ADEOS-1 polarized measurements. *Journal of Geophysical Research: Atmospheres, 106*, 4913-4926, doi:10.1029/2000jd900364

Diner, D.J., Beckert, J.C., Reilly, T.H., Bruegge, C.J., Conel, J.E., Kahn, R.A., Martonchik, J.V.,

Ackerman, T.P., Davies, R., Gerstl, S.A.W., Gordon, H.R., Muller, J.P., Myneni, R.B., Sellers, P.J., Pinty, B., & Verstraete, M.M. (1998). Multi-angle Imaging SpectroRadiometer (MISR) - Instrument description and experiment overview. *Ieee Transactions on Geoscience and Remote Sensing, 36*, 1072-1087, doi:10.1109/36.700992

Dubovik, O., Fuertes, D., Litvinov, P., Lopatin, A., Lapyonok, T., Doubovik, I., Xu, F., Ducos, F., Chen, C., Torres, B., Derimian, Y., Li, L., Herreras-Giralda, M., Herrera, M., Karol, Y., Matar, C., Schuster, G.L., Espinosa, R., Puthukkudy, A., Li, Z., Fischer, J., Preusker, R., Cuesta, J., Kreuter, A., Cede, A., Aspetsberger, M., Marth, D., Bindreiter, L., Hangler, A., Lanzinger, V., Holter, C., & Federspiel, C. (2021). A Comprehensive Description of Multi-Term LSM for Applying Multiple a Priori Constraints in Problems of Atmospheric Remote Sensing: GRASP Algorithm, Concept, and Applications. *Frontiers in Remote Sensing, 2:706851*, doi:10.3389/frsen.2021.706851

Dubovik, O., Herman, M., Holdak, A., Lapyonok, T., Tanre, D., Deuze, J.L., Ducos, F., Sinyuk, A., & Lopatin, A. (2011). Statistically optimized inversion algorithm for enhanced retrieval of aerosol properties from spectral multi-angle polarimetric satellite observations. *Atmospheric Measurement Techniques, 4*, 975-1018, doi:10.5194/amt-4-975-2011

Dubovik, O., & King, M.D. (2000). A flexible inversion algorithm for retrieval of aerosol optical properties from Sun and sky radiance measurements. *Journal of Geophysical Research Atmospheres, 105*, 20673-20696, doi:10.1029/2000JD900282

Dubovik, O., Lapyonok, T., Litvinov, P., Herman, M., Fuertes, D., Ducos, F., Lopatin, A., Chaikovsky, A., Torres, B., Derimian, Y., Huang, X., Aspetsberger, M., & Federspiel, C. (2014). GRASP: a versatile algorithm for characterizing the atmosphere. *SPIE Newsroom*, doi:10.1117/2.1201408.005558

Dubovik, O., Li, Z., Mishchenko, M.I., Tanré, D., Karol, Y., Bojkov, B., Cairns, B., Diner, D.J., Espinosa, W.R., Goloub, P., Gu, X., Hasekamp, O., Hong, J., Hou, W., Knobelspiesse, K.D., Landgraf, J., Li, L., Litvinov, P., Liu, Y., Lopatin, A., Marbach, T., Maring, H., Martins, V., Meijer, Y., Milinevsky, G., Mukai, S., Parol, F., Qiao, Y., Remer, L., Rietjens, J., Sano, I., Stammes, P., Stamnes, S., Sun, X., Tabary, P., Travis, L.D., Waquet, F., Xu, F., Yan, C., & Yin, D. (2019). Polarimetric remote sensing of atmospheric aerosols: Instruments, methodologies, results, and perspectives. *Journal of Quantitative Spectroscopy and Radiative Transfer, 224*, 474-511, doi:10.1016/j.jqsrt.2018.11.024

Dubovik, O., Sinyuk, A., Lapyonok, T., Holben, B.N., Mishchenko, M., Yang, P., Eck, T.F., Volten, H., Munoz, O., Veihelmann, B., van der Zande, W.J., Leon, J.F., Sorokin, M., & Slutsker, I. (2006). Application of spheroid models to account for aerosol particle nonsphericity in remote sensing of desert dust. *Journal of Geophysical Research-Atmospheres, 111*, D11208, doi:10.1029/2005jd006619

Eck, T.F., Holben, B.N., Reid, J.S., Dubovik, O., Smirnov, A., O'Neill, N.T., Slutsker, I., & Kinne, S. (1999). Wavelength dependence of the optical depth of biomass burning, urban, and desert dust aerosols. *Journal of Geophysical Research: Atmospheres, 104*, 31333-31349, doi:10.1029/1999jd900923

Eck, T.F., Holben, B.N., Sinyuk, A., Pinker, R.T., Goloub, P., Chen, H., Chatenet, B., Li, Z., Singh, R.P., Tripathi, S.N., Reid, J.S., Giles, D.M., Dubovik, O., O'Neill, N.T., Smirnov, A., Wang, P., & Xia, X. (2010). Climatological aspects of the optical properties of fine/coarse mode aerosol mixtures. *Journal of Geophysical Research, 115*, D19205, doi:10.1029/2010jd014002

Gao, J., Woodward, A., Vardoulakis, S., Kovats, S., Wilkinson, P., Li, L., Xu, L., Li, J., Yang, J., Li, J., Cao, L., Liu, X., Wu, H., & Liu, Q. (2017). Haze, public health and mitigation measures in China: A review of the current evidence for further policy response. *Science of the Total Environment, 578*, 148-157, doi:https://doi.org/10.1016/j.scitotenv.2016.10.231

Ge, B., Mei, X., Li, Z., Hou, W., Xie, Y., Zhang, Y., Xu, H., Li, K., & Wei, Y. (2020). An improved

algorithm for retrieving high resolution fine-mode aerosol based on polarized satellite data: Application and validation for POLDER-3. *Remote Sensing of Environment, 247*, 111894, doi:10.1016/j.rse.2020.111894

Goloub, P., & Deuze, J.L. (1994). Analysis of the POLDER polarization measurements performed over cloud covers. *IEEE Transactions on Geoscience & Remote Sensing, 32*, 78-88, doi:10.1109/36.285191

Gomez-Chova, L., Camps-Valls, G., Calpe-Maravilla, J., Guanter, L., & Moreno, J. (2007). Cloud-screening algorithm for ENVISAT/MERIS multispectral images. *Ieee Transactions on Geoscience and Remote Sensing, 45*, 4105-4118, doi:10.1109/tgrs.2007.905312

Guo, J., Deng, M., Lee, S.S., Wang, F., Li, Z., Zhai, P., Liu, H., Lv, W., Yao, W., & Li, X. (2016). Delaying precipitation and lightning by air pollution over the Pearl River Delta. Part I: Observational analyses. *Journal of Geophysical Research: Atmospheres, 121*, 6472-6488, doi:10.1002/2015jd023257

Gupta, P., Remer, L.A., Levy, R.C., & Mattoo, S. (2018). Validation of MODIS 3 km land aerosol optical depth from NASA's EOS Terra and Aqua missions. *Atmospheric Measurement Techniques, 11*, 3145-3159, doi:10.5194/amt-11-3145-2018

Hagolle, O., Goloub, P., Deschamps, P.-Y., Cosnefroy, H., Briottet, X., Bailleul, T., Nicolas, J.-M., Parol, F., Lafrance, B., & Herman, M. (1999). Results of POLDER in-flight calibration. *Ieee Transactions on Geoscience and Remote Sensing, 37*, 1550-1566, doi:10.1109/36.763266

Holben, B.N., Eck, T.F., Slutsker, I., Tanre, D., Buis, J.P., Setzer, A., Vermote, E., Reagan, J.A., Kaufman, Y.J., Nakajima, T., Lavenu, F., Jankowiak, I., & Smirnov, A. (1998). AERONET - A federated instrument network and data archive for aerosol characterization. *Remote Sensing of Environment, 66*, 1-16, doi:10.1016/s0034-4257(98)00031-5

Hsu, N.C., Jeong, M.J., Bettenhausen, C., Sayer, A.M., Hansell, R., Seftor, C.S., Huang, J., & Tsay, S.C. (2013). Enhanced Deep Blue aerosol retrieval algorithm: The second generation. *Journal of Geophysical Research: Atmospheres, 118*, 9296-9315, doi:10.1002/jgrd.50712

Hsu, N.C., Tsay, S.C., King, M.D., & Herman, J.R. (2004). Aerosol properties over bright-reflecting source regions. *IEEE Transactions on Geoscience & Remote Sensing, 42*, 557-569, doi:10.1109/TGRS.2004.824067

Jin, S., Ma, Y., Zhang, M., Gong, W., Dubovik, O., Liu, B., Shi, Y., & Yang, C. (2019). Retrieval of 500 m Aerosol Optical Depths from MODIS Measurements over Urban Surfaces under Heavy Aerosol Loading Conditions in Winter. *Remote Sensing, 11*, 2218, doi:10.3390/rs11192218

Jin, S., Zhang, M., Ma, Y., Gong, W., Chen, C., Yang, L., Hu, X., Liu, B., Chen, N., Du, B., & Shi, Y. (2021). Adapting the Dark Target Algorithm to Advanced MERSI Sensor on the FengYun-3-D Satellite: Retrieval and Validation of Aerosol Optical Depth Over Land. *Ieee Transactions on Geoscience and Remote Sensing, 59*, 8781-8797, doi:10.1109/TGRS.2020.3021021

Kacenelenbogen, M., Leon, J.F., Chiapello, I., & Tanre, D. (2006). Characterization of aerosol pollution events in France using ground-based and POLDER-2 satellite data. *Atmospheric Chemistry and Physics, 6*, 4843-4849, doi:10.5194/acp-6-4843-2006

Kaufman, Y.J., Tanré, D., Gordon, H.R., Nakajima, T., Lenoble, J., Frouin, R., Grassl, H., Herman, B.M., King, M.D., & Teillet, P.M. (1997). Passive remote sensing of tropospheric aerosol and atmospheric correction for the aerosol effect. *Journal of Geophysical Research: Atmospheres, 102*, 16815-16830, doi:10.1029/97jd01496

Koren, I., Remer, L.A., Kaufman, Y.J., Rudich, Y., & Martins, J.V. (2007). On the twilight zone between clouds and aerosols. *Geophysical Research Letters, 34*, L08805, doi:10.1029/2007gl029253

Lenoble, J., Remer, L., & Tanre, D. (2013). *Aerosol Remote Sensing*. Springer-Verlag Berlin Heidelberg,

doi:10.1007/978-3-642-17725-5

Levy, R.C., Mattoo, S., Munchak, L.A., Remer, L.A., Sayer, A.M., Patadia, F., & Hsu, N.C. (2013). The Collection 6 MODIS aerosol products over land and ocean. *Atmospheric Measurement Techniques, 6*, 2989-3034, doi:10.5194/amt-6-2989-2013

Li, J.H., Ma, J.J., Li, C., Wang, Y.Y., Li, Z.Q., & Hong, J. (2021). Multi-information collaborative cloud identification algorithm in Gaofen-5 Directional Polarimetric Camera imagery. *Journal of Quantitative Spectroscopy & Radiative Transfer, 261*, 107439, doi:10.1016/j.jqsrt.2020.107439

Li, L., Che, H., Zhang, X., Chen, C., Chen, X., Gui, K., Liang, Y., Wang, F., Derimian, Y., Fuertes, D., Dubovik, O., Zheng, Y., Zhang, L., Guo, B., Wang, Y., & Zhang, X. (2022). A satellite-measured view of aerosol component content and optical property in a haze-polluted case over North China Plain. *Atmospheric Research, 266*, 105958, doi:https://doi.org/10.1016/j.atmosres.2021.105958

Li, L., Dubovik, O., Derimian, Y., Schuster, G.L., Lapyonok, T., Litvinov, P., Ducos, F., Fuertes, D., Chen, C., Li, Z., Lopatin, A., Torres, B., & Che, H. (2019). Retrieval of aerosol components directly from satellite and ground-based measurements. *Atmospheric Chemistry and Physics, 19*, 13409-13443, doi:10.5194/acp-19-13409-2019

Li, X., & Strahler, A.H. (1992). Geometric-optical bidirectional reflectance modeling of the discrete crown vegetation canopy: effect of crown shape and mutual shadowing. *Ieee Transactions on Geoscience and Remote Sensing, 30*, 276-292, doi:10.1109/36.134078

Li, Z., Hou, W., Hong, J., Zheng, F., Luo, D., Wang, J., Gu, X., & Qiao, Y. (2018). Directional Polarimetric Camera (DPC): Monitoring aerosol spectral optical properties over land from satellite observation. *Journal of Quantitative Spectroscopy and Radiative Transfer, 218*, 21-37, doi:10.1016/j.jqsrt.2018.07.003

Li, Z.Q., Lau, W.K.M., Ramanathan, V., Wu, G., Ding, Y., Manoj, M.G., Liu, J., Qian, Y., Li, J., Zhou, T., Fan, J., Rosenfeld, D., Ming, Y., Wang, Y., Huang, J., Wang, B., Xu, X., Lee, S.S., Cribb, M., Zhang, F., Yang, X., Zhao, C., Takemura, T., Wang, K., Xia, X., Yin, Y., Zhang, H., Guo, J., Zhai, P.M., Sugimoto, N., Babu, S.S., & Brasseur, G.P. (2016). Aerosol and monsoon climate interactions over Asia. *Reviews of Geophysics, 54*, 866-929, doi:10.1002/2015rg000500

Liu, B., Ma, X., Ma, Y., Li, H., Jin, S., Fan, R., & Gong, W. (2022). The relationship between atmospheric boundary layer and temperature inversion layer and their aerosol capture capabilities. *Atmospheric Research, 271*, doi:10.1016/j.atmosres.2022.106121

Lopatin, A., Dubovik, O., Fuertes, D., Stenchikov, G., Lapyonok, T., Veselovskii, I., Wienhold, F.G., Shevchenko, I., Hu, Q., & Parajuli, S. (2021). Synergy processing of diverse ground-based remote sensing and in situ data using the GRASP algorithm: applications to radiometer, lidar and radiosonde observations. *Atmos. Meas. Tech., 14*, 2575-2614, doi:10.5194/amt-14-2575-2021

Lyapustin, A., Wang, Y., Korkin, S., & Dong, H. (2018). MODIS Collection 6 MAIAC algorithm. *Atmospheric Measurement Techniques, 11*, 5741-5765, doi:10.5194/amt-11-5741-2018

Ma, Y., Zhu, Y., Liu, B., Li, H., Jin, S., Zhang, Y., Fan, R., & Gong, W. (2021). Estimation of the vertical distribution of particle matter (PM2.5) concentration and its transport flux from lidar measurements based on machine learning algorithms. *Atmospheric Chemistry and Physics, 21*, 17003-17016, doi:10.5194/acp-21-17003-2021

Martins, J.V., Tanré, D., Remer, L., Kaufman, Y., Mattoo, S., & Levy, R. (2002). MODIS Cloud screening for remote sensing of aerosols over oceans using spatial variability. *Geophysical Research Letters, 29*, doi:10.1029/2001GL013252

McCormick, M.P., Hamill, P., Pepin, T.J., Chu, W.P., Swissler, T.J., & McMaster, L.R. (1979).

SATELLITE STUDIES OF THE STRATOSPHERIC AEROSOL. *Bulletin of the American Meteorological Society, 60*, 1038-1046, doi:10.1175/1520-0477(1979)060<1038:ssotsa>2.0.co;2

Mishchenko, M.I., & Travis, L.D. (1997). Satellite retrieval of aerosol properties over the ocean using polarization as well as intensity of reflected sunlight. *Journal of Geophysical Research: Atmospheres, 102*, 16989-17013, doi:https://doi.org/10.1029/96JD02425

Nadal, F., & Bréon, F.M. (1999). Parameterization of Surface Polarized Reflectance Derived from POLDER Spaceborne Measurements. *IEEE Transactions on Geoscience & Remote Sensing, 37*, 1709-1718, doi:10.1109/36.763292

Nakajima, T., Yoon, S.C., Ramanathan, V., Shi, G.Y., Takemura, T., Higurashi, A., Takamura, T., Aoki, K., Sohn, B.J., Kim, S.W., Tsuruta, H., Sugimoto, N., Shimizu, A., Tanimoto, H., Sawa, Y., Lin, N.H., Lee, C.T., Goto, D., & Schutgens, N. (2007). Overview of the Atmospheric Brown Cloud East Asian Regional Experiment 2005 and a study of the aerosol direct radiative forcing in east Asia. *Journal of Geophysical Research-Atmospheres, 112*, 23, doi:10.1029/2007jd009009

Ou, Y., Li, L., Ying, Z., Dubovik, O., Derimian, Y., Chen, C., Fuertes, D., Xie, Y., Lopatin, A., Ducos, F., & Peng, Z. (2021). Spatio-Temporal Variability of Aerosol Components, Their Optical and Microphysical Properties over North China during Winter Haze in 2012, as Derived from POLDER/PARASOL Satellite Observations. *Remote Sensing, 13*, 2682, doi:10.3390/rs13142682

Qie, L., Li, Z., Zhu, S., Xu, H., Xie, Y., Qiao, R., Hong, J., & Tu, B. (2021). In-flight radiometric and polarimetric calibration of the Directional Polarimetric Camera onboard the GaoFen-5 satellite over the ocean. *Appl Opt, 60*, 7186-7199, doi:10.1364/AO.422980

Rao, C.R.N., Stowe, L.L., & McClain, E.P. (1989). REMOTE-SENSING OF AEROSOLS OVER THE OCEANS USING AVHRR DATA THEORY, PRACTICE AND APPLICATIONS. *International Journal of Remote Sensing, 10*, 743-749, doi:10.1080/01431168908903915

Remer, L.A., Mattoo, S., Levy, R.C., Heidinger, A., Pierce, R.B., & Chin, M. (2012). Retrieving aerosol in a cloudy environment: aerosol product availability as a function of spatial resolution. *Atmospheric Measurement Techniques, 5*, 1823-1840, doi:10.5194/amt-5-1823-2012

Rosenfeld, D., Lohmann, U., Raga, G.B., O'Dowd, C.D., Kulmala, M., Fuzzi, S., Reissell, A., & Andreae, M.O. (2008). Flood or drought: How do aerosols affect precipitation? *Science, 321*, 1309-1313, doi:10.1126/science.1160606

Sayer, A.M., Hsu, N.C., Bettenhausen, C., & Jeong, M.J. (2013). Validation and uncertainty estimates for MODIS Collection 6 "Deep Blue" aerosol data. *Journal of Geophysical Research: Atmospheres, 118*, 7864-7872, doi:10.1002/jgrd.50600

Sayer, A.M., Munchak, L.A., Hsu, N.C., Levy, R.C., Bettenhausen, C., & Jeong, M.J. (2014). MODIS Collection 6 aerosol products: Comparison between Aqua's e-Deep Blue, Dark Target, and "merged" data sets, and usage recommendations. *Journal of Geophysical Research-Atmospheres, 119*, 13965-13989, doi:10.1002/2014jd022453

Shi, T., Han, G., Ma, X., Gong, W., Chen, W., Liu, J., Zhang, X., Pei, Z., Gou, H., & Bu, L. (2021). Quantifying CO2 Uptakes Over Oceans Using LIDAR: A Tentative Experiment in Bohai Bay. *Geophysical Research Letters, 48*, e2020GL091160, doi:https://doi.org/10.1029/2020GL091160

Tanre, D., Breon, F.M., Deuze, J.L., Dubovik, O., Ducos, F., Francois, P., Goloub, P., Herman, M., Lifermann, A., & Waquet, F. (2011). Remote sensing of aerosols by using polarized, directional and spectral measurements within the A-Train: the PARASOL mission. *Atmospheric Measurement Techniques, 4*, 1383-1395, doi:10.5194/amt-4-1383-2011

Tegen, I., & Lacis, A.A. (1996). Modeling of particle size distribution and its influence on the radiative

675   properties of mineral dust aerosol. *Journal of Geophysical Research Atmospheres, 101*, 19237-19244,

676   doi:10.1029/95JD03610

677   Zhang, M., Jin, S., Ma, Y., Fan, R., Wang, L., Gong, W., & Liu, B. (2021). Haze events at different levels

678   in winters: A comprehensive study of meteorological factors, Aerosol characteristics and direct radiative

679   forcing in megacities of north and central China. *Atmospheric Environment, 245*, 118056,

680   doi:https://doi.org/10.1016/j.atmosenv.2020.118056

681   Zhdanova, E.Y., Chubarova, N.Y., & Lyapustin, A.I. (2020). Assessment of urban aerosol pollution over

682   the Moscow megacity by the MAIAC aerosol product. *Atmospheric Measurement Techniques, 13*, 877-

683   891, doi:10.5194/amt-13-877-2020

684   Zhu, S., Li, Z., Qie, L., Xu, H., Ge, B., Xie, Y., Qiao, R., Xie, Y., Hong, J., Meng, B., Tu, B., & Chen, F.

685   (2022). In-Flight Relative Radiometric Calibration of a Wide Field of View Directional Polarimetric

686   Camera Based on the Rayleigh Scattering over Ocean. *Remote Sensing, 14*, doi:10.3390/rs14051211

687   Zhu, Z., & Woodcock, C.E. (2012). Object-based cloud and cloud shadow detection in Landsat imagery.

688   *Remote Sensing of Environment, 118*, 83-94, doi:10.1016/j.rse.2011.10.028

689

690
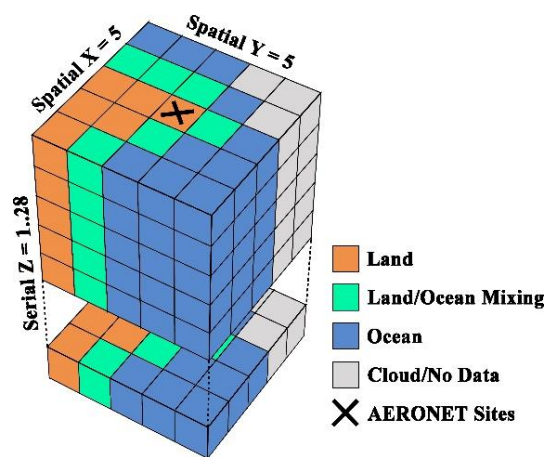
691   **Figure 1.** Schematic diagram for multi-pixel retrieval unit (5×5×1..28). A maximum of 28 sequences

692   allowed in each unit is limited by hardware memory.

693
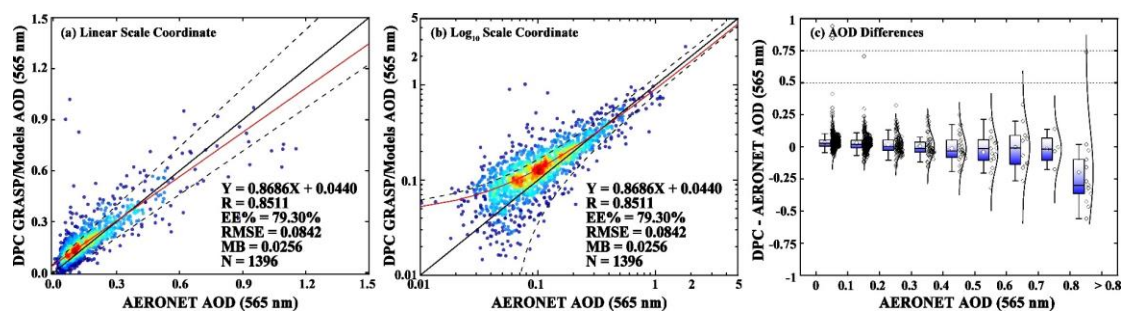
695   **Figure 2. (a)** Density scatterplot of AOD retrievals from DPC with the GRASP/Models scheme

696   versus the AERONET observations with a linear coordinate system. **(b)** The density scatterplot with

697   a logarithmic coordinate system. The solid black line is the one to one and the dashed black lines

698   show the ranges of Expected Error. The red solid lines represent the linear regression line; **(c)** Box

699   plots show changes of differences between DPC GRASP/Models and AEROENT with AOD

700   increasing. Diamond marks and curves represent distributions of sample and normal distribution

701 fitting lines, respectively.
702

704 **Figure 3.** Influencing factors of AOD retrieval performance of DPC based on the GRASP/Models:
705 **(a)** SCA; **(b)** number of viewing angles; **(c)** length of timesteps; **(d)** number of averaged pixels; **(e)**
706 non-polarized fitting residual; **(f)** polarized fitting residual. Orange shadows in the background
707 represents the probability distribution of the samples.
708
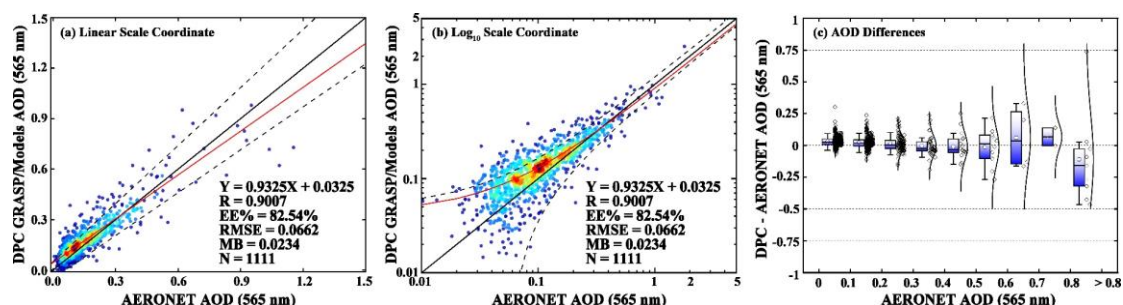
710 **Figure 4. (a)** Density scatterplot of AOD retrievals from DPC with the GRASP/Models scheme
711 versus the AERONET observations with a logarithmic coordinate system after quality control. **(b)**
712 The density scatterplot with a logarithmic coordinate system. The solid black lines are diagonal and
713 the dashed black lines show the ranges of Expected Error. The red solid lines represent the linear
714 regression line; **(c)** Box plots show changes of differences between DPC GRASP/Models and
715 AEROENT with AOD increasing. Diamond marks and curves represent distributions of sample and
716 normal distribution fitting lines, respectively.
717
718

719
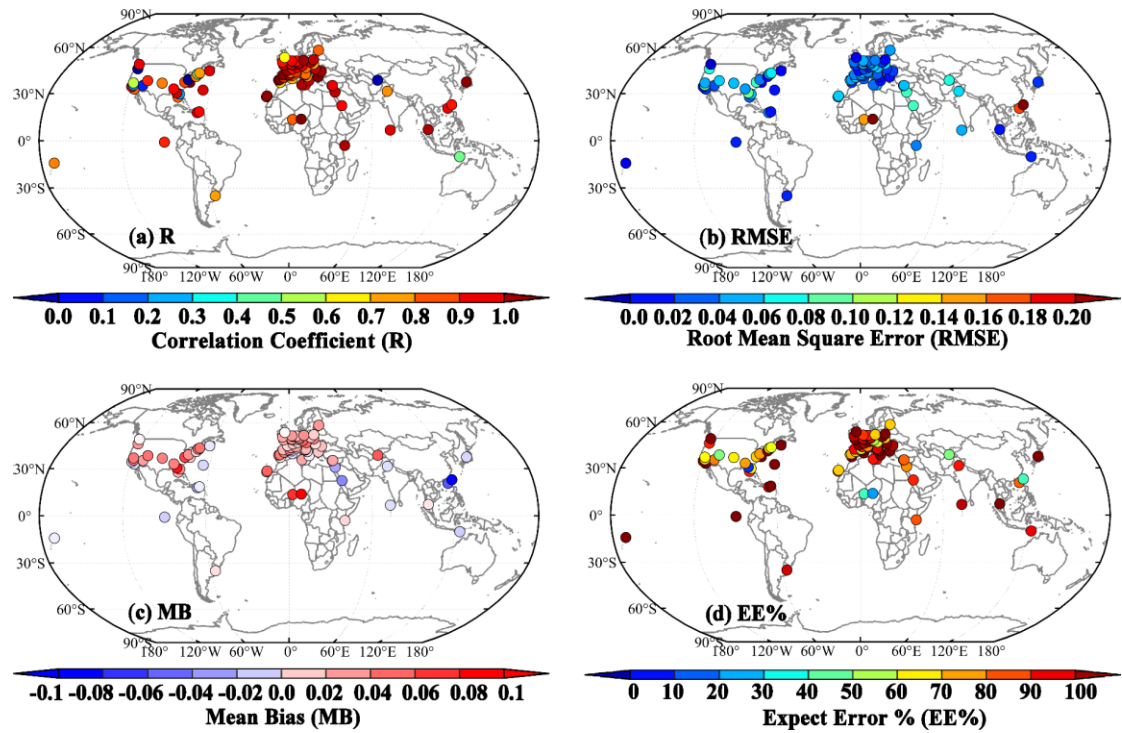
720 **Figure 5**. Spatial Distributions of **(a)** R, **(b)** RMSE**, (c)** MB**,** and **(d)** EE% calculated from DPC
721 GRASP/Models by compared with AERONET observations. Only sites with more than 5 matching
722 points are included.

723

724
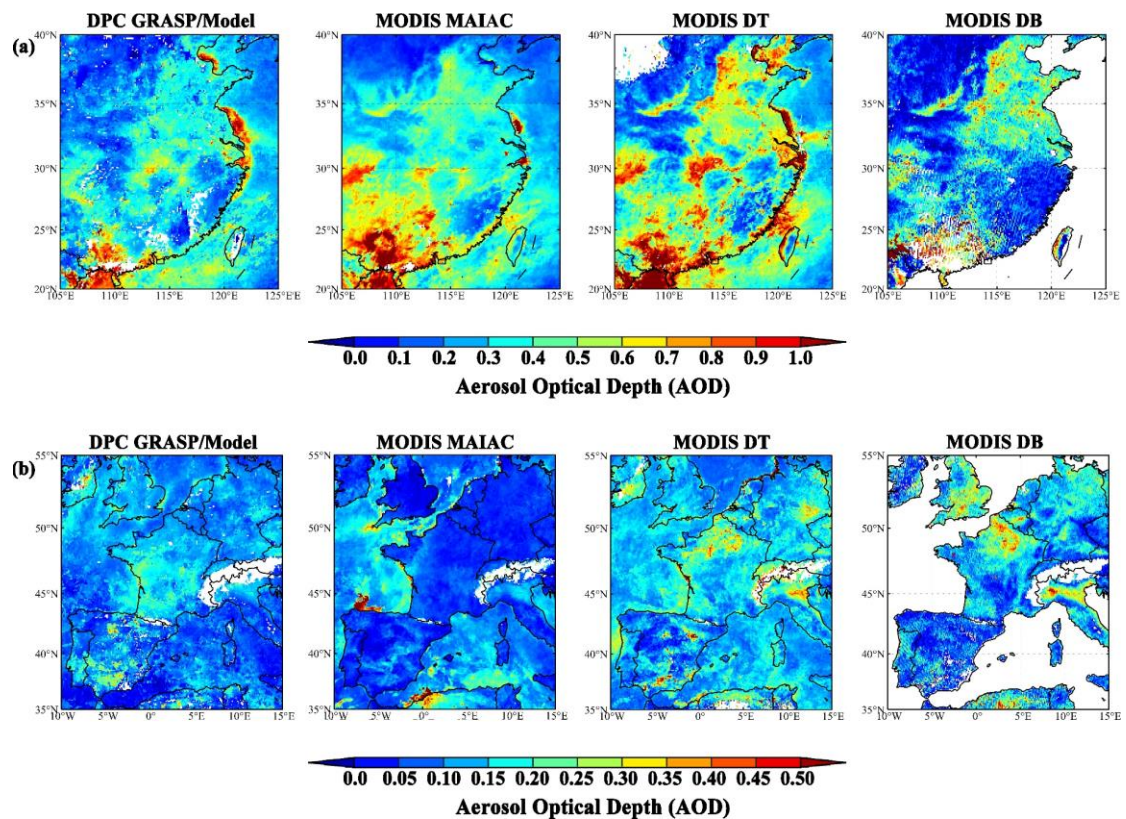
725 **Figure 6**. Spatial distribution of AOD from DPC GRASP/Models compared with MODIS MAIMC,
726 DT, and DB aerosol products in March, 2020: **(a)** Eastern and Southern China with its adjacent sea

 areas; **(b)** Areas of Western Europe including the Atlantic Ocean and the Mediterranean. The DPC

 AOD is at 565 nm and the MODIS AOD is at 550 nm.
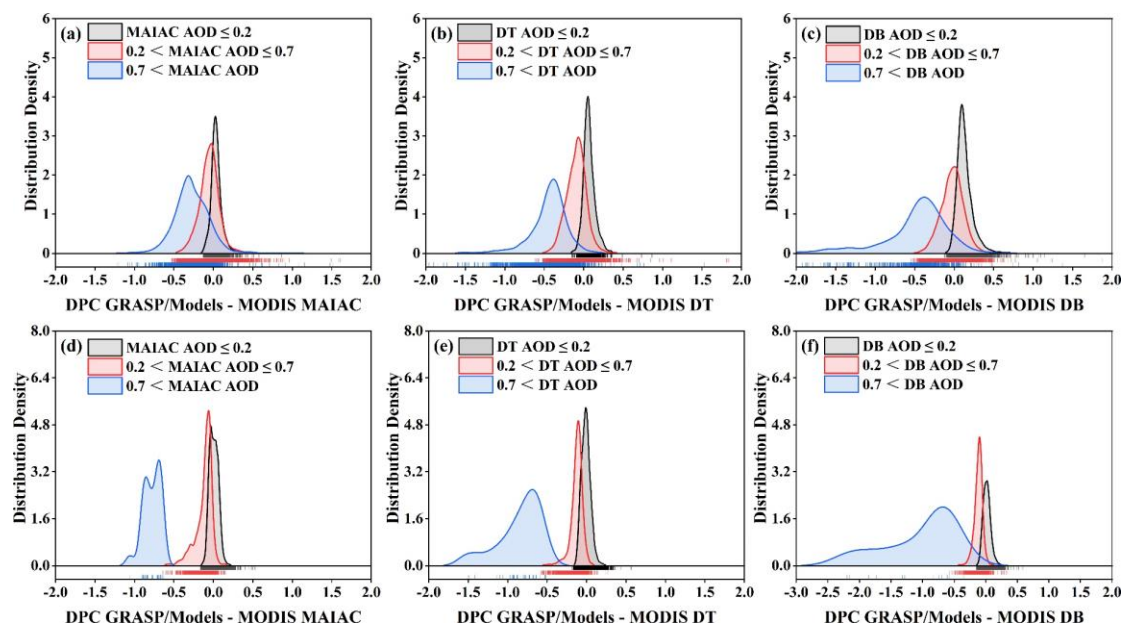
 Figure 7. Distribution Density of AOD differences between DPC GRASP/Models and MODIS DT,

 DB, and MAIAC products at: **(a-c)** Eastern and Southern China with its adjacent sea areas; **(d-e)**

 Areas of Western Europe including the Atlantic Ocean and the Mediterranean. It is noted that the

 MODIS DB product only releases terrestrial AOD data.
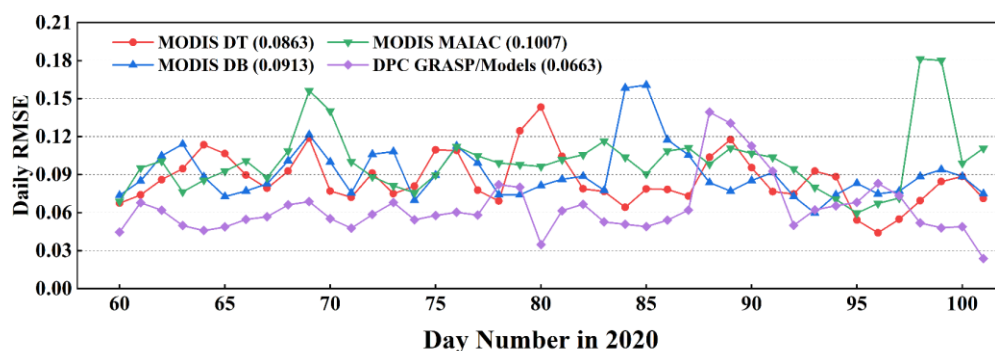
 Figure 8. Time series of daily RMSE for the selected AERONET stations during March and April

 of 2020. The number in brackets are averaged values of daily RMSE. The positions of AERONET

 stations are the same with **Figure 5**.

742
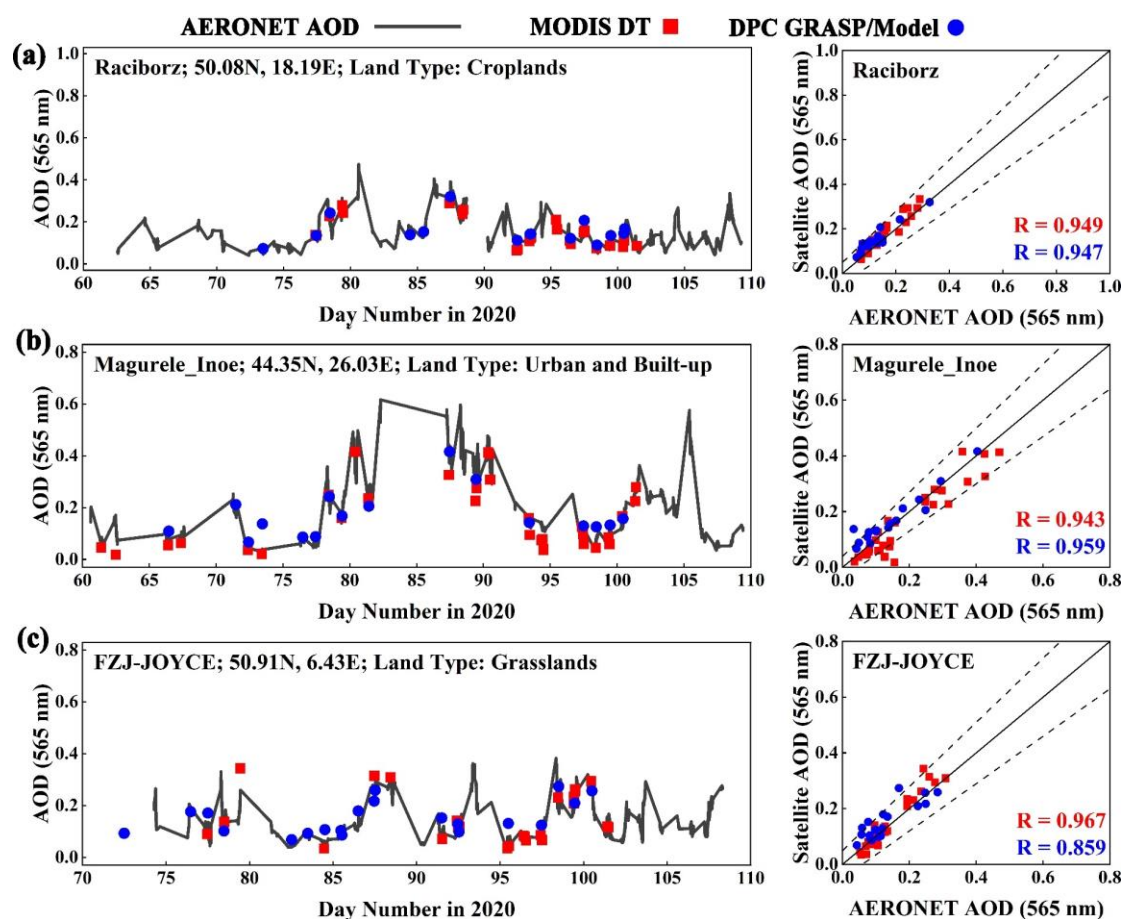
Figure 9. Time series of AOD from the DPC GRASP/Models versus the MODIS DT products and
AERONET observations at three sites as cases: **(a)** Raciborz, **(b)** Magurele_Inoe, and **(c)** FZJ-
JOYCE. The scatterplot shows the relationship between AERONET AOD and satellite AOD.

746